

Domes of T_c in single-band and multiband superconductors with finite-range attractive interactions

Nazim Boudjada, Finn Lasse Buessen , and Arun Paramekanti *

Department of Physics, University of Toronto, Toronto, Ontario M5S1A7, Canada



(Received 18 June 2020; revised 21 July 2020; accepted 23 July 2020; published 6 August 2020)

The rise and fall of the superconducting transition temperature T_c upon tuning carrier density or external parameters, such as pressure or magnetic field, is ubiquitously observed in a wide range of quantum materials. In order to investigate such domes of T_c , we go beyond the prototypical attractive Hubbard model and consider a lattice model of electrons coupled via instantaneous, spatially extended, attractive interactions. By numerically solving the mean-field equations, as well as going beyond mean field theory using a functional renormalization group approach, we find that for a characteristic interaction range ℓ , there exists a dome in T_c around $k_F\ell \sim \mathcal{O}(1)$. For multiband systems, our mean field theory shows the presence of additional domes in the vicinity of Lifshitz transitions. Our results hold in both two and three dimensions and can be intuitively understood from the geometric relation between the Fermi surface and the interaction range. Our model may be relevant for domes of T_c in dilute weakly coupled superconductors or in engineered cold atom systems.

DOI: [10.1103/PhysRevB.102.054504](https://doi.org/10.1103/PhysRevB.102.054504)

I. INTRODUCTION

Domes in the superconducting (SC) transition temperature T_c , observed across a broad range of quantum materials, typically reflect some form of underlying dynamical competition in the electronic fluid. In heavy fermion compounds [1–3] and iron pnictide materials [4–6], for instance, the SC dome emerges around magnetic or nematic quantum critical points (QCPs). In SrTiO_3 , SC domes may possibly be driven by proximity to a ferroelectric QCP [7–18]. In the cuprates, even aside from the physics of QCPs, a decrease in the hole concentration can enhance spin-fluctuation mediated pair formation while simultaneously suppressing the superfluid density as a consequence of Mott physics or competing orders. This interplay yields the highest T_c at an optimal doping [19,20]. SC near QCPs has also been found in numerical simulations and field theory studies [21–27]. Finally, for ultracold atomic fermions, the highest T_c appears near unitary scattering which marks the BCS-BEC crossover from weak to strong coupling SC [28,29].

In this paper, we discuss a geometric picture of superconducting domes in systems with (nonretarded) finite-range attractive interactions. Our proposal is motivated by the following observation. In a system where electrons attract each other over a fixed characteristic range ℓ in real space, the typical momentum transfer in electron-electron scattering processes is $\Delta k \sim 1/\ell$. Thus, in dilute systems with Fermi momentum $k_F \ll \Delta k$, such interactions can efficiently scatter electrons across any two points on the Fermi surface (FS). In the opposite limit, however, when $k_F \gg \Delta k$, the aforementioned interactions lead to small-angle scattering, making it more challenging for electrons to explore the full FS. Therefore, the phase space which is accessible in a single

electron-scattering event initially increases with the size of the FS, before dropping at high densities when the locality of the interactions in momentum space suppresses global SC. Consequently, a domelike dependence of T_c on the electron density emerges around some intermediate Fermi momentum k_F^* which satisfies $k_F^*\ell \sim \mathcal{O}(1)$. The dome thus marks the crossover from predominantly global interactions to local interactions in momentum space. From a real-space perspective, the highest T_c occurs when the interaction range ℓ becomes comparable to the interparticle spacing. Our work does not address the microscopic origin of such a pairing interaction or the length scale ℓ , which are important issues in their own right [14,30–33], but it is reminiscent of the geometric Mott-Ioffe-Regel criterion which marks the crossover from coherent to incoherent electronic transport [34] without reference to an underlying mechanism.

This geometric picture for T_c domes was initially proposed in the context of single-band superconductors [35], where semianalytical expressions of T_c for different scattering potentials were obtained within a weak-coupling mean-field approach. Our study expands on this previous work by presenting numerical solutions to the mean field equations for T_c and the gap over a wide range of densities and coupling strengths for single-band and multiband superconductors in two and three dimensions. In the multiband case, we find the emergence of multiple domes of T_c as new bands get occupied with increasing density. In addition, we use a functional renormalization group (FRG) approach to study the single-band model. We find that including corrections beyond mean field theory suppresses T_c in the low-density regime, yet the maximum in T_c persists. At higher densities near half-filling, where mean field theory predicts a finite T_c , the FRG approach shows that the effective low energy interactions flow towards strong forward scattering, indicating a breakdown of superconductivity. We tentatively identify this breakdown of SC with the onset of phase separation.

*arunp@physics.utoronto.ca

We envision that our results can be applied as a toy model for systems with critical modes or soft bosons which may induce long-range attractive interactions, e.g., fermions experiencing fluctuating zero-momentum orders. We thus make some qualitative comparisons with results on dilute electron gases in bulk SrTiO₃. Previous work has also discussed how density-dependent screening might lead to domes of T_c in SrTiO₃ [31–33]. Models similar in spirit to our study have also previously been explored in the context of cuprates [36], SrTiO₃ [18,35], FeSe on SrTiO₃ [37,38], and ultracold atomic fermions [39]. Our work may also be relevant to ultracold Bose-Fermi mixtures, where ℓ could be set by the correlation length associated with the superfluid to Mott insulator transition [40]. We emphasize, however, that the T_c dome we uncover is not inherently a strong-coupling phenomenon so that mean field theory and our (truncated) FRG approach are expected to provide genuine insight.

II. MODEL HAMILTONIAN

We consider a tight-binding Hamiltonian parametrized as

$$\mathcal{H}_0 = \sum_{\mathbf{k}\mu\nu} c_\mu^\dagger(\mathbf{k}) H_0^{\mu\nu}(\mathbf{k}) c_\nu(\mathbf{k}), \quad (1)$$

where μ, ν stand for generic orbital and spin indices which give a matrix structure to the Hamiltonian H_0 . The electrons are assumed to interact via an instantaneous attractive interaction

$$\mathcal{H}_{\text{int}} = \frac{1}{2} \int d^d \mathbf{r} \int d^d \mathbf{r}' \mathcal{V}(\mathbf{r} - \mathbf{r}') \hat{n}(\mathbf{r}) \hat{n}(\mathbf{r}'), \quad (2)$$

with $\hat{n}(\mathbf{r}) = \sum_\mu c_\mu^\dagger(\mathbf{r}) c_\mu(\mathbf{r})$ being the density operator at position \mathbf{r} , and $\mathcal{V}(\mathbf{r} - \mathbf{r}') < 0$ being the interaction potential.

Anticipating a singlet superconducting instability, we Fourier transform the interaction to momentum space and focus on the zero center of mass pairing channel, which leads to the effective Hamiltonian

$$\mathcal{H}_{\text{int}}^{\text{BCS}} = \frac{1}{2N} \sum_{\mathbf{k}\mathbf{k}'} c_\mu^\dagger(\mathbf{k}) c_\nu^\dagger(-\mathbf{k}) V(\mathbf{k} - \mathbf{k}') c_\nu(-\mathbf{k}') c_\mu(\mathbf{k}'), \quad (3)$$

where N is the total number of lattice sites and summation over repeated indices is implied. The interaction $V(\mathbf{k} - \mathbf{k}')$ is the Fourier transform of $\mathcal{V}(\mathbf{r} - \mathbf{r}')$. We decouple the interaction, using a Hubbard-Stratonovich transformation, via complex bosonic fields $\Delta_{\mu\nu}(\mathbf{k})$ and integrate out the fermions (see Appendix A for details). The resulting self-consistent matrix gap equation is given by

$$\Delta(\mathbf{k}) = -\frac{1}{N} \sum_{\mathbf{k}'} V(\mathbf{k} - \mathbf{k}') U(\mathbf{k}') \frac{\tanh \left[\frac{E(\mathbf{k}')}{2T} \right]}{2E(\mathbf{k}')} U^\dagger(\mathbf{k}') \Delta(\mathbf{k}'), \quad (4)$$

where T is the temperature, $E(\mathbf{k})$ is a diagonal matrix comprising the square roots of the eigenvalues of $H_0(\mathbf{k}) H_0^\dagger(\mathbf{k}) + \Delta(\mathbf{k}) \Delta^\dagger(\mathbf{k})$, and $U(\mathbf{k})$ is the corresponding eigenvector matrix. For a one-band model this expression reduces to the familiar single-gap equation. We assume a Gaussian interaction $\mathcal{V}(\mathbf{r}) = -g_0 e^{-|\mathbf{r}|^2/2\ell^2}$, so that $V(\mathbf{q}) = -g_0 (2\pi\ell^2)^{d/2} e^{-|\mathbf{q}|^2\ell^2/2}$ in d spatial dimensions [41]. Here $g_0 > 0$ is the pairing strength, and ℓ sets the range of the potential in real space (in units of the lattice constant).

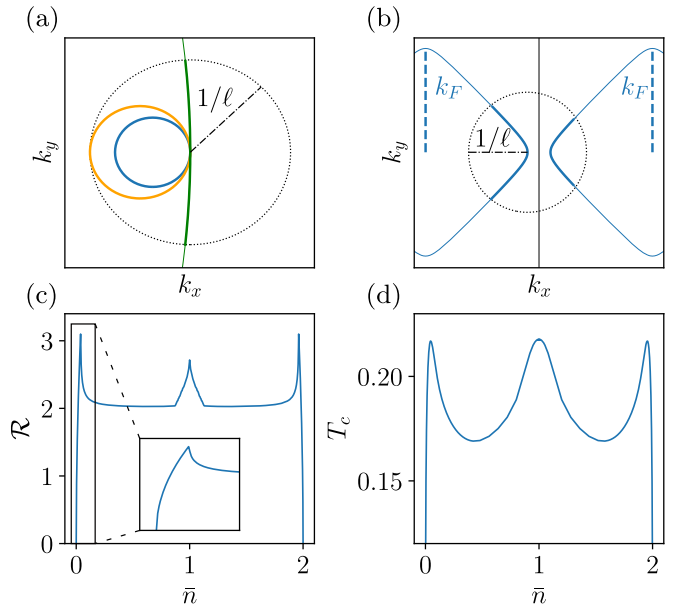


FIG. 1. (a) Schematic picture showing a reference momentum point on different FSs of increasing sizes (blue, orange, green). Thick lines indicate the geometrically accessible parts of the FS within the scattering circle of radius $1/\ell$. (b) Same as previous panel, but for larger Fermi surfaces (blue) where Umklapp scattering becomes relevant near the BZ boundary. (c) Arc length $\mathcal{R}(\bar{n})$ of the accessible part of the FS as a function of electron density \bar{n} , plotted for $\ell = 1$. Inset: \mathcal{R} at low density showing a scaling $\sim \sqrt{\bar{n}}$. (d) T_c as a function of \bar{n} for a 2D square lattice for a fixed interaction range $\ell = 5$, showing peaks at the densities $\bar{n} \approx 0.04, 1, 1.96$ (see text for details).

For $\ell \rightarrow 0$, the interaction reduces to a Hubbard model, while a large value of ℓ favors small momentum scattering. We note that it has already been pointed out for the single-band case that the results remain qualitatively unchanged even for alternative potentials [35], such as a Lorentzian or a hard sphere, with a similar characteristic range ℓ . To explore the full density dependence and multiband examples, we numerically solve the gap equation for T_c and the momentum dependence of the gap $\Delta_{\mu\nu}(\mathbf{k})$. For a fixed density \bar{n} , we also simultaneously solve for the chemical potential.

III. SINGLE BAND SUPERCONDUCTOR

We begin by discussing the geometric origin of domes of T_c for interactions with finite range ℓ in a single-band superconductor. As illustrated in Fig. 1(a), for a given momentum point on the 2D FS, the arc length \mathcal{R} of the FS [42] which lies within the (momentum-space) interaction range $\sim 1/\ell$ depends on the electron density. Starting from the dilute limit, up to $k_F \ell = 1/2$, the full FS circumference $2\pi k_F$ is accessible in a single electron-scattering event [which implies a scaling $\mathcal{R} \sim k_F$ in the dilute limit, cf. inset of Fig. 1(c)]. Beyond this value, the accessible part of the FS shrinks to $2/\ell < 2\pi k_F$ at large k_F . Upon further increasing the density towards half-filling (i.e., when $\bar{n} \sim 1$), Umklapp processes become allowed and the scattering phase space is enhanced again for $|\mathbf{k}_F - (\mathbf{k}'_F \pm \mathbf{G})|/\ell = 1$ where \mathbf{G} is a reciprocal lattice vector. This is shown pictorially in Fig. 1(b).

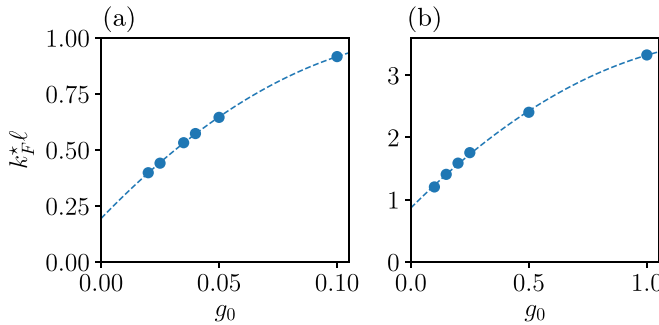


FIG. 2. Value of $k_F \ell$ at the geometric peak of T_c as a function of coupling g_0 in (a) 2D and (b) and 3D. Extrapolation (dashed lines) to the weak-coupling limit $g_0 \rightarrow 0$ suggests that $k_F^* \ell \rightarrow 0.20$ in 2D and $k_F^* \ell \rightarrow 0.86$ in 3D. In 3D, $k_F^* \ell$ is larger than in 2D, indicating that the dome of T_c is shifted towards lower densities, whereas the peak value of T_c remains comparable in both dimensions. This is in part due to the difference in density of states at low filling.

where the accessible scattering region for a point on the left BZ includes also states from the right BZ. Finally, when $\bar{n} \gg 1$, there exists yet another geometric peak arising from small hole pockets near (π, π) . Consequently, as seen in Fig. 1(c), the functional form of $\mathcal{R}(\bar{n})$ for a 2D square lattice with dispersion $\xi(\mathbf{k}) = -2t_1(\cos(k_x) + \cos(k_y)) - \mu$ and $\ell = 1$ exhibits three sharp peaks: at a low density n^* corresponding to $k_F \ell = 1/2$, at half-filling $\bar{n} = 1$, and at $2 - n^*$. Since \mathcal{R} is a geometric measure of the available phase space [43] for Cooper pairs, we expect the peak in \mathcal{R} to be reflected as a dome in T_c .

Although this simple geometric argument which neglects the energy dependence of the density of states does not predict a peak of T_c in 3D, we shall demonstrate that a smoothed version of this geometric maximum generally persists. To illustrate this in a simple one-band example, we compute the mean-field singlet pairing T_c using $\ell = 5$ and $g_0 = 1$ (in units of t_1), observing a peak in T_c at an electron density $n^* \approx 0.04$ in the dilute limit as shown in Fig. 1(d). At higher densities, T_c exhibits the same additional peaks as predicted by $\mathcal{R}(\bar{n})$. We point out that the middle peak stems from a combination of an increased geometric overlap with states in the second BZ and an enhanced density of states near the van Hove singularity.

Our numerical solution of the gap equation shows that domes of T_c also appear in 3D. To investigate the role of the coupling strength g_0 in the occurrence of the dome, we compute $k_F^* \ell$ as a function of g_0 , where k_F^* is the angle-averaged Fermi wave vector associated with the density n^* [44]. The results for the 2D square lattice as well as for the 3D cubic lattice show that the dome shifts towards smaller densities as g_0 is reduced, see Fig. 2. However, we emphasize that the dome persists at a nonzero density even in the very weak coupling limit. Indeed, extrapolating our results to $g_0 \rightarrow 0$, we find a finite value $k_F^* \ell \approx 0.20$ in 2D and $k_F^* \ell \approx 0.86$ in 3D. At the same time, the ratio of the critical temperature and the Fermi energy T_c^*/ϵ_F^* at the geometric peak remains moderate (with $T_c^*/\epsilon_F^* < 1$ for $g_0 = 1$, and decreasing for smaller g_0), implying that the dome is not a strong-coupling phenomenon.

When $k_F \ell \gg 1$, we note that many angular momentum pairing channels become quasidegenerate as seen from the

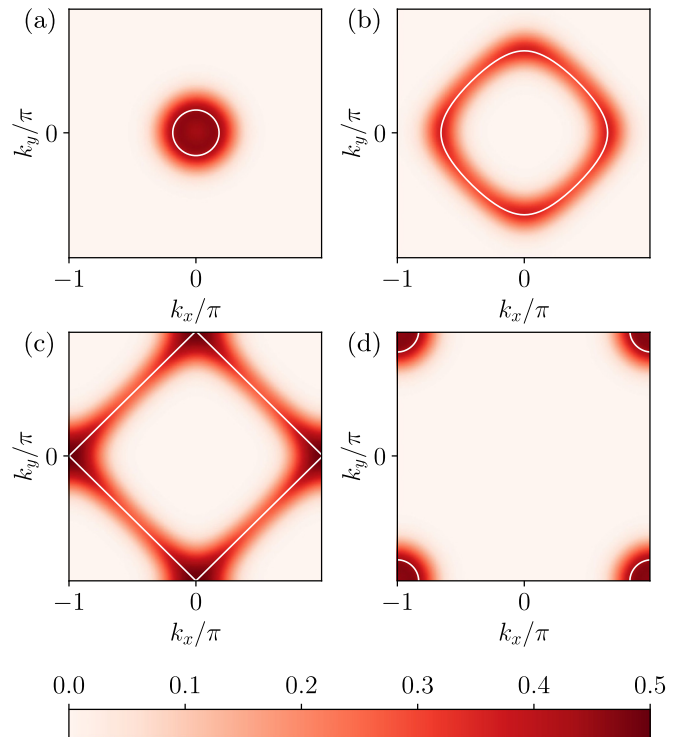


FIG. 3. Zero temperature solution $|\Delta(\mathbf{k})|$ (in units of $t_1 = 1$) to the nonlinear gap equation at different densities. (a) In the electron dilute limit ($\bar{n} = 0.04$), the gap is peaked at the Γ point while (b) at intermediate densities ($\bar{n} = 0.6$) it peaks around the FS. (c) At half-filling, the gap reaches its maximum at the van Hove points ($\bar{n} = 1$) and (d) in the dilute hole regime ($\bar{n} = 1.96$) the maximum is at the M points.

eigenfunctions of the subleading instabilities in the linearized mean-field gap equation (see Appendix B). However, the dominant instability is for an “s-wave” gap with no nodes. Similar results were found in the context of superconductivity mediated by charge-density wave [45] and nematic quantum critical points [46,47].

In Fig. 3, we plot the gaps obtained by solving the nonlinear gap equation at $T = 0$ for various densities. In the low electron density [panel (a)] or hole density [panel (d)] regimes, the gap peaks at the center of the small electron FS or small hole FS (i.e., at the Γ and M points, respectively). At intermediate densities, however, the weight of the gap is distributed on the FS in the radial direction, decaying $\sim 1/\ell$ away from \mathbf{k}_F . In addition, the gap shows a subdominant modulation over the FS, being larger along the $k_x = 0$ and $k_y = 0$ lines than along the zone diagonals. This modulation becomes more apparent near half-filling as the FS approaches the van Hove singularity.

IV. MULTIBAND SUPERCONDUCTOR

We next generalize our mean-field results to multiband examples and demonstrate that the geometric interpretation of domes still holds. Furthermore, we shall see that in multiband systems, it is possible to obtain multiple domes of T_c as new FSs appear with increasing density. To this end, we consider

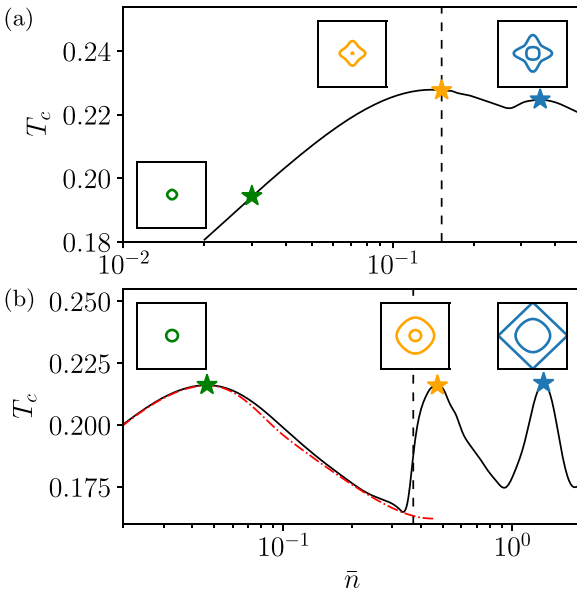


FIG. 4. Superconducting transition temperature T_c for a two-orbital model showing a double geometric peak in the low-density regime. Colored stars correspond to the FSs in the insets. Vertical dashed line marks the Lifshitz transition when the second band appears at the Fermi level. (a) Two hybridized elliptical FSs (b) two circular FSs with a finite potential difference (black curve). For comparison, we also show the result from a single orbital model (red curve) which reproduces the first peak in T_c .

the two-orbital model

$$\mathcal{H}_0 = \sum_{\mathbf{k}\sigma} (a_{\mathbf{k}\sigma}^\dagger \quad b_{\mathbf{k}\sigma}^\dagger) \begin{pmatrix} \xi_a(\mathbf{k}) + V_0 & \delta \\ \delta & \xi_b(\mathbf{k}) - V_0 \end{pmatrix} \begin{pmatrix} a_{\mathbf{k}\sigma} \\ b_{\mathbf{k}\sigma} \end{pmatrix}, \quad (5)$$

where $\xi_a(\mathbf{k}) = -2t_1 \cos(k_x) - 2t_2 \cos(k_y) - \mu$ and $\xi_b(\mathbf{k}) = -2t_2 \cos(k_x) - 2t_1 \cos(k_y) - \mu$, with δ and V_0 being the momentum-independent interorbital hybridization and potential difference, respectively.

To study the impact of interorbital hybridization, we set $t_1=1$, $\ell=5$, and $g_0=1$, and choose, for illustrative purposes, $t_2=\delta=0.2$. This choice corresponds to two elliptical bands which hybridize to produce C_4 symmetric FSs. In the low-density regime ($\bar{n} \ll 0.1$), only one band crosses the Fermi level and the physics is analogous to the single orbital model, i.e., a geometric dome forms at a density corresponding to the optimal value of $k_F \ell$ [orange star in Fig. 4(a)]. The parameters are chosen such that the Lifshitz transition, i.e., the appearance of the second band at the Fermi level, occurs near the maximum of the dome. The second band then gives rise to a second geometric peak at a slightly higher density (blue star), yielding an overall double peak structure. We note, however, that for different parameter choices, the Lifshitz transition does not necessarily coincide with the first peak in T_c : For example, increasing ℓ pushes the geometric peak to lower densities [so that $k_F^* \ell \sim \mathcal{O}(1)$] but has no impact on the Lifshitz transition point.

Next, we study the impact of a finite potential difference between the two orbitals, keeping $\delta=0$ and setting $t_2=V_0=1$. This corresponds to two C_4 symmetric bands separated in energy by $2V_0$. The two orbitals are only coupled via the

constraint of the total density being fixed. In Fig. 4(b), we plot T_c with the Fermi surfaces at the three peak densities in electron-doped regime shown in the insets and the dashed red curve showing the one-orbital model with the same parameters. In the low-density regime, the two curves agree exactly, showing that only the lower band dictates T_c : A first geometric peak (marked by a green star) is reached at $\bar{n} = n^* \approx 0.04$ which corresponds to $k_F^* \ell \approx 2.85$. Near the Lifshitz transition of the two-band model (vertical dashed curve), the one-orbital and two-orbital models start to diverge since the higher energy band crosses the Fermi level and starts to contribute to T_c . A second geometric peak (orange star) is reached precisely when the Fermi wave vector of the new band is such that $k_F^* \ell \approx 2.85$. At higher densities, the lower energy band reaches the van Hove point and we see the corresponding van Hove peak (blue star). As in the case of the one-orbital model, particle-hole symmetry dictates $T_c(\bar{n}) = T_c(4 - \bar{n})$ and an exact copy of the three peaks is obtained in the hole-doped regime $\bar{n} > 2$.

V. FUNCTIONAL RG APPROACH

In deriving the gap equation Eq. (4), we have explicitly assumed Cooper pair formation in the singlet channel. While yielding a structurally simple, self-consistent mean-field theory, the decoupling comes at the price of being inherently biased to favor the specific type of superconductivity encoded in the ansatz, potentially neglecting any competing phases. For $k_F \ell \gg 1$, as pointed out earlier, different patches on the FS could effectively decouple as many angular momentum pairing channels become quasidegenerate. Furthermore, attractive interactions could make the system unstable towards phase separation. Such effects can lead to a breakdown of coherent superconductivity.

To investigate this breakdown—or, conversely, justify the mean-field ansatz—we employ an FRG approach which treats all competing interaction channels on equal footing [48–50]. The resulting FRG flow equations, which relate the bare interaction as defined in Eq. (2) to an effective low-energy theory by continuously tracing its evolution under infinitesimal reductions of the temperature [51], naturally have a more complex structure than the self-consistent mean-field equation and in general cannot be solved exactly. For weak coupling, however, it is sufficient to include only the one-loop contributions to the flow equations for the two-particle interaction, neglecting higher-order processes [52], and to treat the interaction vertex in a momentum patching approximation which resolves the angular component of the momentum dependence around the FS. In this way, a finite set of differential equations is obtained which can be solved numerically to determine the effective interaction vertex $u_T(n_1, n_2, n_3)$, where the n_i enumerate the momentum patches around the FS. The specific choice of momentum patches, as well as the detailed FRG flow equations, are outlined in Appendix D. We have benchmarked our FRG calculations using the attractive Hubbard model.

We now discuss our FRG calculations on the single-band model with finite range interactions for fixed $\ell=1$ and $g_0=\frac{3}{2\pi}$, while varying the density \bar{n} to assess the role of competing interaction channels. The RG flow is initialized at an upper temperature $T_{\max} = 4t_1$, which is comparable to

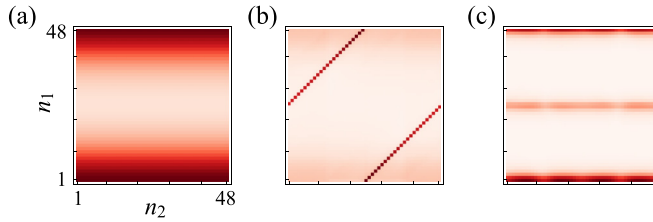


FIG. 5. Effective interaction in the patching approximation. Normalized color code shows the value of the flowing interaction vertex $u_T(n_1, n_2, 1)$, where (n_1, n_2) enumerate momentum patches around the FS. (a) Density $\bar{n}=0.17$ at $T=T_{\max}$, (b) $\bar{n}=0.17$ at $T=T_{\min}$, (c) $\bar{n}=0.94$ at $T=T_{\min}$.

the bandwidth, and stopped at a temperature scale T_{\min} when the maximum component of the vertex exceeds $18t_1$, which is large compared to the bandwidth. The onset of strong interactions at T_{\min} can then be related to a putative phase transition [53]. We point out that the attractive Gaussian model we consider here with $\ell=1$ is similar to an extended Hubbard model, and a peak of T_c is indeed observed in both models [54].

In the dilute limit, $k_F\ell \ll 1$, the bare interaction at $T=T_{\max}$ has negligible momentum dependence on the FS. The Gaussian profile becomes visible only at slightly larger \bar{n} as seen in Fig. 5(a). The effective low-temperature vertex, however, for a wide range of \bar{n} is dominated by a pronounced interaction between momentum patches which lie on opposite sides of the FS. The sign structure of this effective low-energy action is uniformly attractive, which indicates impending zero-momentum Cooper pair formation and s-wave superconductivity [55], see Fig. 5(b). However, at large densities $\bar{n} > 0.88$, the initial Gaussian profile of the bare interaction sharpens throughout the RG flow as shown in Fig. 5(c), so that the renormalized $\ell \rightarrow \infty$, and forward scattering gets enhanced. The isolated limit of forward scattering has previously been shown to cause an instability of the Fermi liquid [56]. Here, the breakdown of Cooper pairing and coherent superconductivity occurs as the low energy limit of a realistic finite range model over an extended regime of electron densities.

We study the role of additional interaction channels in the breakdown by comparing the full FRG calculations with reduced flow equations that only include the particle-particle forward scattering as also captured by the mean-field ansatz. We find that we can divide the FRG phase diagram shown in Fig. 6 into three regimes. In regime I ($\bar{n} < 0.58$) the superconducting T_c is suppressed by fluctuations in additional interaction channels. Nevertheless, as shown in the inset to Fig. 6, the full FRG calculation yields a dome of T_c , in qualitative agreement with the simplified mean-field approach. In regime II ($0.58 < \bar{n} < 0.88$) on the other hand, unlike what is seen for the attractive Hubbard model, the finite-range character of the interactions leads to an enhancement of T_{\min} by the additional interaction channels. Finally, in regime III ($\bar{n} > 0.88$), mean-field theory formally yields a finite T_c , while the full FRG approach reveals the breakdown of superconductivity. We tentatively identify this regime, where the renormalized $\ell \rightarrow \infty$, with phase separation induced by extended attractive interactions.

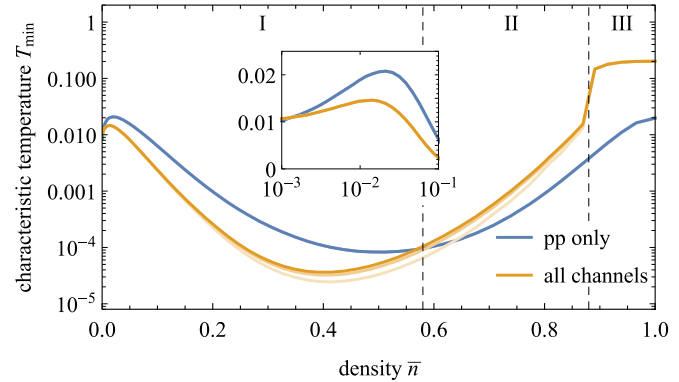


FIG. 6. Characteristic temperature T_{\min} for the Gaussian interaction potential with $\ell=1$, as determined from FRG calculations which include only particle-particle scattering (blue curve) or all interaction channels (orange curve). Curves plotted in opaque colors are computed using $N_p=96$ momentum patches, curves in lighter colors are for $N_p=72$ and $N_p=48$. In regimes I and II, the effective vertex at T_{\min} captures superconducting pairing, while in regime III the interaction becomes increasingly localized in momentum space leading to a breakdown of SC. Inset shows the geometric dome of T_c at low density.

VI. CONCLUSION

We have provided a geometric phase space argument for the formation of T_c domes in systems with spatially extended interactions. We have shown that for multiband systems a scenario with two or more domes can arise naturally. In order to apply this picture to 3D bulk SrTiO₃, we note that the first dome with maximum transition temperature $T_c \approx 0.2$ K is centered at a density $\bar{n} \approx 1.2 \times 10^{18}$ cm⁻³ with a Fermi energy $\epsilon_F \approx 2$ meV. Demanding $k_F\ell \sim 1$ at the center of the dome yields $\ell \sim 30$ Å, while requiring $T_c/\epsilon_F \sim 10^{-2}$ at this point fixes $g_0 \sim 4.5$ meV. The inferred length scale ℓ may reflect the range of attractive interactions between polaron quasiparticles which have been reported in bulk SrTiO₃ [57] and its interfaces [58,59]. The microscopic theory of SC of such dilute polarons remains an open issue. It would be interesting to explore such T_c domes in a wider range of experimental systems including atomic Bose-Fermi mixtures and to extend the FRG results by incorporating the frequency dependence of the interaction vertex. Such studies may also shed light on the interplay of spatially extended interactions with retardation effects in driving SC near QCPs.

ACKNOWLEDGMENTS

We thank M. M. Scherer and Y. Kedem for discussions. This work was funded by NSERC of Canada and FRQNT of Quebec. The numerical simulations were performed on the JURECA cluster at the Forschungszentrum Juelich, and on the Cedar and Niagara clusters enabled by support provided by Compute Ontario, SciNet, Westgrid, and Compute Canada. SciNet is funded by: the Canada Foundation for Innovation, the Government of Ontario, Ontario Research Fund - Research Excellence, and the University of Toronto.

APPENDIX A: DERIVATION OF MULTIBAND GAP EQUATION

We start by writing the imaginary-time action for free fermions:

$$S_0 = \frac{1}{V^2} \int d^d \mathbf{r} \int d^d \mathbf{r}' \int_0^\beta d\tau \bar{\psi}_\mu(\mathbf{r}, \tau) [\partial_\tau \delta_{\mu\nu} - H_0^{\mu\nu}(\mathbf{r}, \mathbf{r}')] \psi_\nu(\mathbf{r}', \tau), \quad (\text{A1})$$

where $V = Na^d$ is the volume of the d -dimensional cubic system with N sites of lattice constant a . Working in units where $a = 1$, we can Fourier transform S_0 to momentum and Matsubara frequency space for a translationally invariant system:

$$\begin{aligned} S_0 &= \frac{1}{N} \sum_{\mathbf{k}\omega_n} \bar{\psi}_\mu(\mathbf{k}, i\omega_n) [\mathrm{i}\omega_n \delta_{\mu\nu} - H_0^{\mu\nu}(\mathbf{k})] \psi_\nu(\mathbf{k}, i\omega_n) \\ &= \frac{1}{2N} \sum_{\mathbf{k}\omega_n} \left(\bar{\psi}_\mu(\mathbf{k}, i\omega_n) \underbrace{[\mathrm{i}\omega_n \delta_{\mu\nu} - H_0^{\mu\nu}(\mathbf{k})]}_{G_{0p}^{-1}(\mathbf{k}, i\omega_n)} \psi_\nu(\mathbf{k}, i\omega_n) + \psi_\mu(-\mathbf{k}, -i\omega_n) \underbrace{[\mathrm{i}\omega_n \delta_{\mu\nu} + H_0^{\nu\mu}(-\mathbf{k})]}_{G_{0h}^{-1}(-\mathbf{k}, -i\omega_n)} \bar{\psi}_\nu(-\mathbf{k}, -i\omega_n) \right) \\ &= \frac{1}{2N} \sum_{\mathbf{k}\omega_n} (\bar{\psi}(\mathbf{k}, i\omega_n) \quad \psi(-\mathbf{k}, -i\omega_n)) \begin{pmatrix} G_{0p}^{-1}(\mathbf{k}, i\omega_n) & 0 \\ 0 & G_{0h}^{-1}(-\mathbf{k}, -i\omega_n) \end{pmatrix} \begin{pmatrix} \psi(\mathbf{k}, i\omega_n) \\ \bar{\psi}(-\mathbf{k}, -i\omega_n) \end{pmatrix}, \end{aligned} \quad (\text{A2})$$

where G_{0p}^{-1} and G_{0h}^{-1} are the matrix noninteracting Green's functions, neglecting self-energy corrections. The instantaneous interaction is, in real space:

$$S_{\text{int}} = \frac{1}{2V^2} \int d^d \mathbf{r} \int d^d \mathbf{r}' \int_0^\beta d\tau \bar{\psi}_\mu(\mathbf{r}, \tau) \bar{\psi}_\nu(\mathbf{r}', \tau) \mathcal{V}(\mathbf{r} - \mathbf{r}') \psi_\nu(\mathbf{r}', \tau) \psi_\mu(\mathbf{r}, \tau), \quad (\text{A3})$$

and in \mathbf{k} space, if we only keep zero center of mass momentum terms:

$$S_{\text{int}} = \frac{1}{2\beta N^2} \sum_{\mathbf{k}\mathbf{k}'} \sum_{\omega_n \omega_m} \bar{\psi}_\mu(\mathbf{k}, i\omega_n) \bar{\psi}_\nu(-\mathbf{k}, -i\omega_n) V(\mathbf{k} - \mathbf{k}') \psi_\nu(-\mathbf{k}', -i\omega_m) \psi_\mu(\mathbf{k}', i\omega_m), \quad (\text{A4})$$

with $V(\mathbf{k} - \mathbf{k}') < 0$ the Fourier transform of $\mathcal{V}(\mathbf{r})$. We now introduce the complex fields $\Delta_{\mu\nu}(\mathbf{k})$:

$$\begin{aligned} e^{-S_{\text{int}}} &\propto \int \mathcal{D}[\bar{\Delta}, \Delta] \exp \left(-\frac{1}{2N} \sum_{\mathbf{k}\omega_n} \left(\frac{\beta}{N} \sum_{\mathbf{k}'} \Delta_{\mu\nu}(\mathbf{k}') \Delta_{\nu\mu}^*(\mathbf{k}) F(\mathbf{k} - \mathbf{k}') \right. \right. \\ &\quad \left. \left. + \psi_\nu(-\mathbf{k}, -i\omega_n) \Delta_{\nu\mu}^*(\mathbf{k}) \psi_\mu(\mathbf{k}, i\omega_n) + \bar{\psi}_\mu(\mathbf{k}, i\omega_n) \Delta_{\mu\nu}(\mathbf{k}) \bar{\psi}_\nu(-\mathbf{k}, -i\omega_n) \right) \right) \end{aligned} \quad (\text{A5})$$

with $F(\mathbf{k} - \mathbf{k}') = \frac{1}{V} \int d^d \mathbf{r} \frac{e^{i(\mathbf{k}-\mathbf{k}') \cdot \mathbf{r}}}{\mathcal{V}(\mathbf{r})}$. The total partition function, $\mathcal{Z} = \int \mathcal{D}[\bar{\psi}, \psi] e^{-(S_0 + S_{\text{int}})}$ up to normalization constants, becomes quadratic in the fermion fields:

$$\begin{aligned} \mathcal{Z} &= \int \mathcal{D}[\bar{\Delta}, \Delta] \exp \left(-\frac{\beta}{2N^2} \sum_{\mathbf{k}\mathbf{k}'} \Delta_{\mu\nu}(\mathbf{k}') \Delta_{\nu\mu}^*(\mathbf{k}) F(\mathbf{k} - \mathbf{k}') \right) \\ &\times \int \mathcal{D}[\bar{\psi}, \psi] \exp \left(-\frac{1}{2N} \sum_{\mathbf{k}\omega_n} (\bar{\psi}(\mathbf{k}, i\omega_n) \quad \psi(-\mathbf{k}, -i\omega_n)) \underbrace{\begin{pmatrix} G_{0p}^{-1}(\mathbf{k}, i\omega_n) & \Delta(\mathbf{k}) \\ \Delta^\dagger(\mathbf{k}) & G_{0h}^{-1}(-\mathbf{k}, -i\omega_n) \end{pmatrix}}_{\mathcal{G}^{-1}(\mathbf{k}, i\omega_n)} \underbrace{\begin{pmatrix} \psi(\mathbf{k}, i\omega_n) \\ \bar{\psi}(-\mathbf{k}, -i\omega_n) \end{pmatrix}}_{\Psi(\mathbf{k}, i\omega_n)} \right). \end{aligned} \quad (\text{A6})$$

We can proceed by integrating out the fermions and obtain the effective action $\mathcal{Z} = \int \mathcal{D}[\bar{\Delta}, \Delta] e^{-S_{\text{eff}}}$:

$$S_{\text{eff}} = \underbrace{\frac{\beta}{2N^2} \sum_{\mathbf{k}\mathbf{k}'} \Delta_{\mu\nu}(\mathbf{k}') \Delta_{\nu\mu}^*(\mathbf{k}) F(\mathbf{k} - \mathbf{k}')}_{S_1} + \underbrace{\frac{1}{2N} \sum_{\mathbf{k}\omega_n} \text{tr} \log \begin{pmatrix} i\omega_n \mathbb{I} - H_0(\mathbf{k}) & \Delta(\mathbf{k}) \\ \Delta^\dagger(\mathbf{k}) & i\omega_n \mathbb{I} + H_0^\dagger(-\mathbf{k}) \end{pmatrix}}_{S_2}. \quad (\text{A7})$$

To obtain the equation of motion, we need to set $\frac{\delta S_{\text{eff}}}{\delta \Delta_{\sigma\lambda}^*(\mathbf{p})} = 0$. Varying S_1 is straightforward:

$$\frac{1}{\beta} \frac{\delta S_1}{\delta \Delta_{\sigma\lambda}^*(\mathbf{p})} = \frac{1}{2N^2} \sum_{\mathbf{k}\mathbf{k}'} \delta_{\nu\sigma} \delta_{\mu\lambda} \delta^{(d)}(\mathbf{p} - \mathbf{k}) \Delta_{\mu\nu}(\mathbf{k}') F(\mathbf{k} - \mathbf{k}') = \frac{1}{2N} \sum_{\mathbf{k}'} \Delta_{\lambda\sigma}(\mathbf{k}') F(\mathbf{p} - \mathbf{k}'). \quad (\text{A8})$$

Varying S_2 leads to:

$$\begin{aligned} \frac{1}{\beta} \frac{\delta S_2}{\delta \Delta_{\sigma\lambda}^*(\mathbf{p})} &= \frac{1}{2\beta N} \sum_{\mathbf{k}\omega_n} \text{tr} \left(\frac{\delta \log(\mathcal{G}^{-1}(\mathbf{k}, i\omega_n))}{\delta \mathcal{G}^{-1}(\mathbf{k}, i\omega_n)} \frac{\delta \mathcal{G}^{-1}(\mathbf{k}, i\omega_n)}{\delta \Delta_{\sigma\lambda}^*(\mathbf{p})} \right) \\ &= \frac{1}{2\beta N} \sum_{\mathbf{k}\omega_n} \left[\mathcal{G}(\mathbf{k}, i\omega_n) \delta^{(d)}(\mathbf{p} - \mathbf{k}) \begin{pmatrix} 0 & 0 \\ \delta_{\sigma\lambda} & 0 \end{pmatrix} \right] \\ &= \frac{1}{2\beta} \sum_{\omega_n} [\mathcal{G}(\mathbf{p}, i\omega_n)]_{\lambda\sigma}^{12}. \end{aligned} \quad (\text{A9})$$

$[\mathcal{G}(\mathbf{p}, i\omega_n)]_{\lambda\sigma}^{12}$ refers to the (λ, σ) matrix element of the (1,2) block (i.e., top right block) of the \mathcal{G} matrix. In order to invert a matrix containing square block matrices, we make use of the following identity:

$$\begin{pmatrix} A & B \\ C & D \end{pmatrix}^{-1} = \begin{pmatrix} A^{-1} + A^{-1}B(D - CA^{-1}B)^{-1}CA^{-1} & -A^{-1}B(D - CA^{-1}B)^{-1} \\ -(D - CA^{-1}B)^{-1}CA^{-1} & (D - CA^{-1}B)^{-1} \end{pmatrix}. \quad (\text{A10})$$

Focusing on the top right corner, we obtain after some algebra and using the particle-hole symmetry of the Hamiltonian:

$$\begin{aligned} [\mathcal{G}(\mathbf{p}, i\omega_n)]^{12} &= -[\omega_n^2 + i\omega_n(H_0(\mathbf{p}) - \Delta(\mathbf{p})H_0^T(-\mathbf{p})\Delta^{-1}(\mathbf{p})) + \Delta(\mathbf{p})H_0^T(-\mathbf{p})\Delta^{-1}(\mathbf{p})H_0(\mathbf{p}) + \Delta(\mathbf{p})\Delta^\dagger(\mathbf{p})]^{-1}\Delta(\mathbf{p}) \\ &= -(i\omega_n\mathbb{I} - \mathcal{E}(\mathbf{p}))^{-1}(i\omega_n\mathbb{I} + \mathcal{E}(\mathbf{p}))^{-1}\Delta(\mathbf{p}) \end{aligned} \quad (\text{A11})$$

and $\mathcal{E}^2(\mathbf{p}) \equiv H_0(\mathbf{p})H_0^\dagger(\mathbf{p}) + \Delta(\mathbf{p})\Delta^\dagger(\mathbf{p})$. This matrix can be diagonalized via $\mathcal{E}^2(\mathbf{p}) = U(\mathbf{p})E^2(\mathbf{p})U^\dagger(\mathbf{p})$ and the Matsubara frequency summation performed:

$$\begin{aligned} \frac{1}{\beta} \frac{\delta S_2}{\delta \Delta_{\sigma\lambda}^*(\mathbf{p})} &= \frac{1}{2\beta} \sum_{i\omega_n} -(i\omega_n\mathbb{I} - \mathcal{E}(\mathbf{p}))_{\sigma m}^{-1}(i\omega_n\mathbb{I} + \mathcal{E}(\mathbf{p}))_{m\alpha}^{-1}\Delta_{\alpha\lambda}(\mathbf{p}) \\ &= -\frac{1}{2\beta} \sum_{i\omega_n} U_{\sigma m}(\mathbf{p})(i\omega_n - E(\mathbf{p}))_m^{-1}(i\omega_n + E(\mathbf{p}))_m^{-1}U_{m\alpha}^*(\mathbf{p})\Delta_{\alpha\lambda}(\mathbf{p}) \\ &= \frac{1}{2} U_{\sigma m}(\mathbf{p}) \frac{1}{2E_m(\mathbf{p})} \tanh\left(\frac{\beta E_m(\mathbf{p})}{2}\right) U_{m\alpha}^*(\mathbf{p})\Delta_{\alpha\lambda}(\mathbf{p}) \end{aligned} \quad (\text{A12})$$

with implied sums over repeated indices. In matrix notation:

$$\frac{1}{\beta} \frac{\delta S_{\text{eff}}}{\delta \Delta^\dagger(\mathbf{p})} = \frac{1}{2N} \sum_{\mathbf{k}'} F(\mathbf{p} - \mathbf{k}')\Delta(\mathbf{k}') + \frac{1}{2} U(\mathbf{p}) \frac{1}{2E(\mathbf{p})} \tanh\left(\frac{\beta E(\mathbf{p})}{2}\right) U^\dagger(\mathbf{p})\Delta(\mathbf{p}) = 0. \quad (\text{A13})$$

For an inversion symmetric scattering potential $\mathcal{V}(\mathbf{r}) = \mathcal{V}(-\mathbf{r})$, this can be rewritten in terms of the Fourier transform $V(\mathbf{k})$:

$$\begin{aligned} \Delta_{\mu\nu}(\mathbf{k}) &= -\frac{1}{N} \sum_{\mathbf{k}'} \sum_{m\lambda} V(\mathbf{k} - \mathbf{k}') U_{\mu m}(\mathbf{k}') \frac{1}{2E_m(\mathbf{k}')} \tanh\left(\frac{E_m(\mathbf{k}')}{2T}\right) U_{m\lambda}^*(\mathbf{k}') \Delta_{\lambda\nu}(\mathbf{k}') \\ &= \sum_{\mathbf{k}'} V(\mathbf{k} - \mathbf{k}') M_{\mu\lambda}(\mathbf{k}') \Delta_{\lambda\nu}(\mathbf{k}'), \end{aligned} \quad (\text{A14})$$

with $M_{\mu\lambda}(\mathbf{k}') \equiv -\frac{1}{N} \sum_m U_{\mu m}(\mathbf{k}') \frac{1}{2E_m(\mathbf{k}'')} \tanh\left(\frac{E_m(\mathbf{k}'')}{2T}\right) U_{m\lambda}^*(\mathbf{k}'')$. Numerically, it is useful to write this as a matrix equation at temperature T :

$$\vec{\Delta}(T) = \mathcal{M}(T) \vec{\Delta}(T) \iff \Delta_i(T) = \mathcal{M}_{ij}(T)\Delta_j(T). \quad (\text{A15})$$

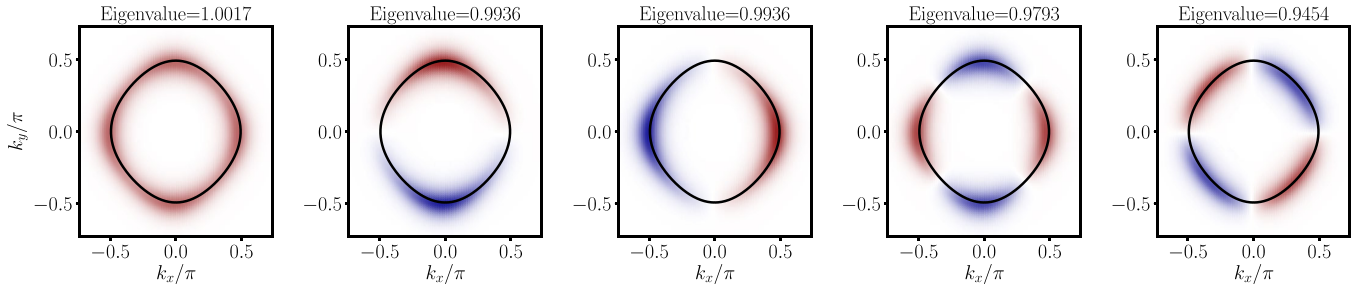


FIG. 7. Eigenvectors of \mathcal{M} with their corresponding eigenvalues at $T = T_c \approx 0.164$ for $(t_1, t_2, g_0, \ell, \bar{n}) = (1, 1, 1, 5, 0.36)$. The Fermi surface is shown in black, while the color map goes from blue (negative) to red (positive), with white being zero intensity. The largest eigenvalue corresponds to lowest energy state.

For a Hamiltonian comprising b bands and discretized on a momentum mesh with N points, the indices $i, j \in [1, \dots, b^2N]$ which makes the matrix \mathcal{M} of dimensions $b^2N \times b^2N$. More explicitly:

$$\begin{pmatrix} \Delta_{11}(\mathbf{k}_1) \\ \Delta_{12}(\mathbf{k}_1) \\ \vdots \\ \Delta_{1b}(\mathbf{k}_1) \\ \vdots \\ \Delta_{bb}(\mathbf{k}_1) \\ \vdots \\ \Delta_{bb}(\mathbf{k}_N) \end{pmatrix} = \begin{pmatrix} V(\mathbf{k}_1 - \mathbf{k}_1)[M(\mathbf{k}_1)] \otimes \mathbb{I}_b & V(\mathbf{k}_1 - \mathbf{k}_2)[M(\mathbf{k}_2)] \otimes \mathbb{I}_b & \dots & V(\mathbf{k}_1 - \mathbf{k}_N)[M(\mathbf{k}_N)] \otimes \mathbb{I}_b \\ V(\mathbf{k}_2 - \mathbf{k}_1)[M(\mathbf{k}_1)] \otimes \mathbb{I}_b & V(\mathbf{k}_2 - \mathbf{k}_2)[M(\mathbf{k}_2)] \otimes \mathbb{I}_b & \dots & V(\mathbf{k}_2 - \mathbf{k}_N)[M(\mathbf{k}_N)] \otimes \mathbb{I}_b \\ \vdots & \vdots & \ddots & \vdots \\ V(\mathbf{k}_N - \mathbf{k}_1)[M(\mathbf{k}_1)] \otimes \mathbb{I}_b & V(\mathbf{k}_N - \mathbf{k}_2)[M(\mathbf{k}_2)] \otimes \mathbb{I}_b & \dots & V(\mathbf{k}_N - \mathbf{k}_N)[M(\mathbf{k}_N)] \otimes \mathbb{I}_b \end{pmatrix} \begin{pmatrix} \Delta_{11}(\mathbf{k}_1) \\ \Delta_{12}(\mathbf{k}_1) \\ \vdots \\ \Delta_{1b}(\mathbf{k}_1) \\ \vdots \\ \Delta_{bb}(\mathbf{k}_1) \\ \vdots \\ \Delta_{bb}(\mathbf{k}_N) \end{pmatrix}, \quad (\text{A16})$$

where \mathbb{I}_b is the $b \times b$ identity matrix.

At $T = T_c$, $E_m(\mathbf{k}) \rightarrow \xi_m(\mathbf{k})$ and $U_{\mu m}(\mathbf{k}) \rightarrow W_{\mu m}(\mathbf{k})$ where $\xi_m(\mathbf{k}) = W_{m\lambda}^*(\mathbf{k})H_0^{\lambda\sigma}(\mathbf{k})W_{\sigma m}(\mathbf{k})$ such that M no longer depends on Δ . Equation (A16) reduces to an eigenvalue equation and T_c is obtained when the largest eigenvalue of \mathcal{M} reaches 1 (for $T \ll T_c$ all the eigenvalues are larger than 1 while for $T \gg T_c$ all the eigenvalues vanish.)

At $T = 0$, the equation is nonlinear as the matrix M depends on Δ and we must solve by (i) guessing an initial $\Delta^{(0)}(\mathbf{k})$, (ii) diagonalizing $H_0(\mathbf{k})H_0^\dagger(\mathbf{k}) + \Delta^{(0)}(\mathbf{k})[\Delta^{(0)}(\mathbf{k})]^\dagger = U(\mathbf{k})[E^{(0)}(\mathbf{k})]^2U^{-1}(\mathbf{k}')$, (iii) constructing the \mathcal{M} matrix and (iv) multiplying by the ‘vectorized’ $\tilde{\Delta}^{(0)}$ to obtain a new vector $\tilde{\Delta}^{(1)}$ which can then be used to repeat the procedure. The gap function $\Delta(T = 0)$ is the ‘fixed point’ of this equation.

Finally, since the instability is expected near the Fermi momenta (i.e., where the denominator $E_m(\mathbf{k}) \rightarrow 0$) it is useful to only store momenta within a given range of \mathbf{k}_F . The length scale ℓ^{-1} provides a natural cutoff and we found that only keeping momenta within $\pm 3\ell^{-1}$ of \mathbf{k}_F is sufficient to reach convergent results.

APPENDIX B: EIGENFUNCTIONS OF THE GAP EQUATION

At $T = T_c$, the spectrum of \mathcal{M} tells us about the eigenmodes of the gap. The largest eigenvalue is the lowest energy state into which the system will condense first and the corresponding eigenvector shows the momentum dependence of the gap. When $\ell \rightarrow \infty$, all eigenvalues converge to 1 and the corresponding eigenvectors become localized to single momentum points on the Fermi surface. In that case, any linear combination of the eigenvectors would be a solution to the gap equation and all momenta condense simultaneously. However, for finite values of ℓ , we generally have one eigenvalue reaching unity before the others. The subleading instabilities become closer to the leading instability at high densities (as this is equivalent to increasing ℓ). For a given density and pairing length scale shown in Fig. 7, we show that the largest eigenvalue is nondegenerate and has *s*-wave symmetry, while the next eigenvalues are doubly degenerate

with p_x and p_y symmetry and the next two have *d*-wave symmetry.

APPENDIX C: ANISOTROPIC DISPERSIONS AND ℓ DEPENDENCE

As we tune the value of ℓ we observe that as ℓ is increased the location of the geometric peak moves to lower densities as expected (thus keeping $k_F^* \ell \sim 1$). On the other hand, although the van Hove peak remains at half filling [Fig. 8(a)], its tail gets sharper for small ℓ because Umklapp scattering only kicks in at increasingly large fillings. For an anisotropic FS with dispersion $\xi(\mathbf{k}) = -2t_1 \cos(k_x) - 2t_2 \cos(k_y) - \mu$ and $t_1 \neq t_2$, the location of the van Hove peak shifts to lower densities since the elongated part of the elliptical FS hits the BZ boundary at densities $\bar{n} < 1$. For a very elliptical FS ($t_2/t_1 \ll 1$ or $t_2/t_1 \gg 1$), the van Hove point is at smaller densities and k_F acquires a strong angular modulation $k_F^{\text{long}} \gg k_F^{\text{short}}$. In turn,

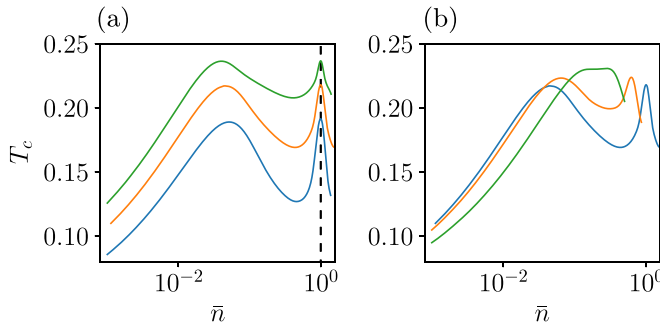


FIG. 8. Critical temperature T_c as a function of electron density \bar{n} for (a): $\ell = 3$ (blue), $\ell = 5$ (orange), and $\ell = 10$ (green). The dashed vertical line at $\bar{n} = 1$ shows, in contrast to the geometric peak, that the location of the van Hove peak doesn't depend on ℓ . In (b), we observe the two peaks merge as the FS is made increasingly anisotropic, going from $t_2 = t_1$ (blue) to $t_2 = 0.5t_1$ (orange) to $t_2 = 0.1t_1$ (green).

this introduces a new condition that as soon as $k_F^{\text{long}}\ell \gg 1$, the available phase space for scattering starts to decrease even if $k_F^{\text{long}}\ell \lesssim 1$. In this scenario, the van Hove peak shifts to lower densities while the geometric peak is pushed to higher densities and the two eventually merge into a single peak [Fig. 8(b)].

APPENDIX D: FRG FLOW EQUATIONS

The general form of the effective two-particle interaction vertex is given by

$$V(K'_1, K'_2; K_1, K_2), \quad (\text{D1})$$

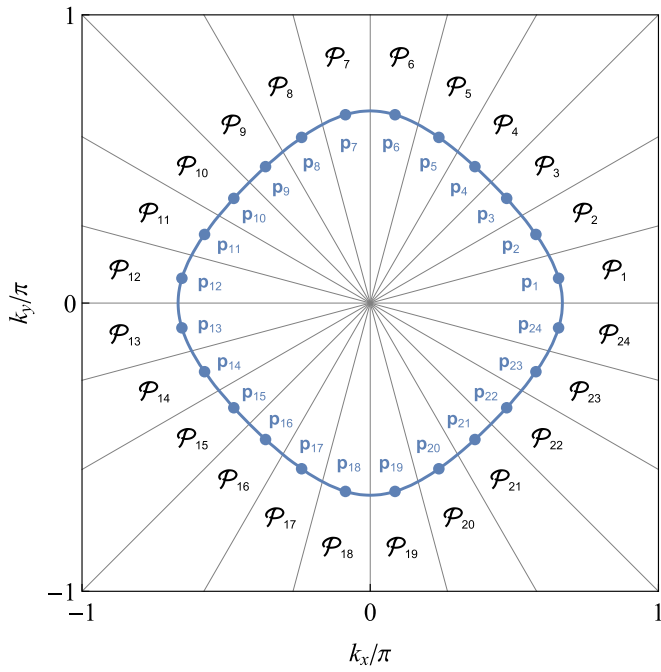


FIG. 9. Partitioning of the Brillouin zone into a set of patches $\mathcal{P}_1, \dots, \mathcal{P}_N$, illustrated for $N = 24$. All momentum points within a single patch \mathcal{P}_m are projected onto the representative momentum \mathbf{p}_m which lies on the Fermi surface.



FIG. 10. Diagrammatic representation of contributions to the flow of the effective interaction. Singling out particle-particle scattering (first term) is equivalent to a Bethe-Salpeter like resummation and generates results on the level of self-consistent mean-field theory. The inclusion of additional direct particle-hole (terms two to four) and crossed particle-particle (last term) scattering allows to model the interplay of competing interaction channels.

where the parameters K_n are composite indices denoting tuples $(\mathbf{k}_n, \omega_n, \alpha_n)$ of momentum, Matsubara frequency, and spin, respectively. In this most general form, the fermionic interaction vertex must be antisymmetric under the pairwise exchange of its arguments. For the SU(2)-symmetric model at hand, however, it is more convenient to constrain the effective interaction to a form which is inherently encoded to be SU(2) symmetric; to this end, we parametrize the effective interaction by two terms—spin-conserving and spin-exchange terms—which span a full basis for SU(2) invariant interactions:

$$\begin{aligned} V(K'_1, K'_2; K_1, K_2) = & U(k'_1, k'_2; k_1, k_2) \delta_{\alpha'_1 \alpha_1} \delta_{\alpha'_2 \alpha_2} \\ & - U(k'_1, k'_2; k_2, k_1) \delta_{\alpha'_1 \alpha_2} \delta_{\alpha'_2 \alpha_1}. \end{aligned} \quad (\text{D2})$$

Here, the composite indices k_n denote pairs (\mathbf{k}_n, ω_n) of momentum and Matsubara frequency, while the spin index α is written out explicitly. The basis function $U(k'_1, k'_2; k_1, k_2)$ is symmetric under simultaneous exchange of ingoing and outgoing indices.

For further simplification of the vertex parametrization we resort to the momentum space patching approximation outlined in Ref. [52], which is suitable in the weak coupling limit. In this approximation, the frequency dependence of the vertex is neglected, while the momentum dependence is parametrized such that it resolves the angular dependence around the Fermi surface, but it neglects any dependence in the radial direction. This is achieved by partitioning the Brillouin zone into a set of patches $\{\mathcal{P}_1 \dots \mathcal{P}_N\}$ as shown in

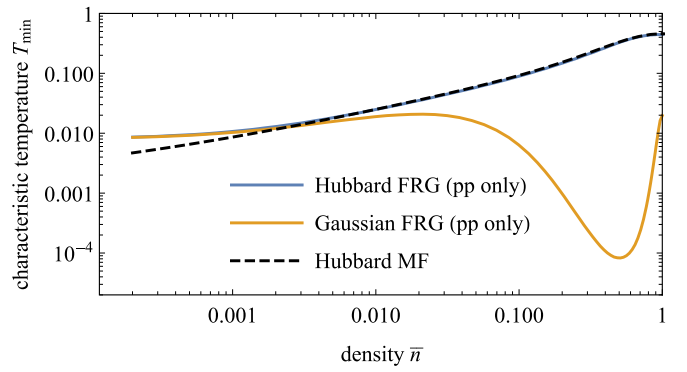


FIG. 11. Benchmark of the characteristic temperature T_{\min} , as determined in FRG calculations (including only particle-particle scattering channel), with the mean-field critical temperature of the Hubbard model. The Hubbard limit $\ell = 0$ shows excellent agreement for fillings $\bar{n} \gtrsim 10^{-3}$. The generalized Gaussian potential ($\ell = 1$) approaches the Hubbard limit in the very dilute regime.

Fig. 9 and projecting all momentum points within a patch \mathcal{P}_m onto a single representative point \mathbf{p}_m on the Fermi surface, i.e., the vertex function is assumed to be constant within the entire patch. The parametrization of the vertex function can thus be written as

$$U(k'_1, k'_2; k_1, k_2) = \sum_{i_1, i_2, i_3} u(n_{i_1}, n_{i_2}, n_{i_3}) \\ \times \delta(\mathbf{k}'_1 + \mathbf{k}'_2 - \mathbf{k}_1 - \mathbf{k}_2) \delta_{\mathbf{k}'_1 \in \mathcal{P}_{i_1}} \delta_{\mathbf{k}'_2 \in \mathcal{P}_{i_2}} \delta_{\mathbf{k}_1 \in \mathcal{P}_{i_3}}, \quad (D3)$$

where the indices n_m enumerate momentum patches and the symbol $\delta_{q \in \mathcal{P}_n} = 1$ if momentum q lies within patch \mathcal{P}_n and zero otherwise.

The FRG flow equations are obtained by introducing an additional dependence of the interaction vertex on some RG cutoff. We follow the temperature flow RG scheme outlined in Ref. [51], where the temperature itself assumes the role of the RG cutoff and the flow equations take the form

$$\frac{d}{dT} u_T(n_1, n_2, n_3) = \mathcal{T}_{PP,T} + \mathcal{T}_{PH,T}^d + \mathcal{T}_{PH,T}^c, \quad (D4)$$

where the three interaction channels (particle-particle, direct particle-hole, and crossed particle-hole interaction, respectively) are given by (terms in the same order as shown in Fig. 10)

$$\begin{aligned} \mathcal{T}_{PP,T}(n_1, n_2, n_3) &= - \sum_n L_T^+(n, n_1 + n_2) \\ &\times u_T(n_1, n_2, n) u_T(n, -n + n_1 + n_2, n_3) \\ \mathcal{T}_{PH,T}^d(n_1, n_2, n_3) &= - \sum_n L_T^-(n, n_1 - n_3) \\ &\times (-2u_T(n_1, n, n_3) u_T(n + n_1 - n_3, n_2, n) \\ &+ u_T(n_1, n, n + n_1 - n_3) u_T(n + n_1 - n_3, n_2, n) \\ &+ u_T(n_1, n, n_3) u_T(n_2, n + n_1 - n_3, n)) \\ \mathcal{T}_{PH,T}^c(n_1, n_2, n_3) &= - \sum_n L_T^-(n, n_2 - n_3) \\ &\times u_T(n_1, n + n_2 - n_3, n) u_T(n, n_2, n_3). \end{aligned} \quad (D5)$$

The internal propagator bubble is defined as

$$L_T^\pm(n, m) = \int_{\mathbf{k} \in \mathcal{P}_n} \mp \frac{\lambda(\xi(\mathbf{k})) \pm \lambda(\xi(\mp \mathbf{k} + \mathbf{p}_m))}{\xi(\mathbf{k}) \pm \xi(\mp \mathbf{k} + \mathbf{p}_m)}, \quad (D6)$$

where $\xi(\mathbf{k})$ is the dispersion of the noninteracting system and $\lambda(\xi)$ is the temperature derivative of the Fermi distribution function $\lambda(\xi) = \xi e^{\xi/T} [T^2(e^{\xi/T} + 1)^2]^{-1}$. In this form, the flow equations can be solved numerically to connect the high-temperature limit, in which the effective interaction vertex Eq. (D1) equals the bare interaction as defined by the Hamiltonian \mathcal{H}_{int} , to the effective low-energy theory.

APPENDIX E: HUBBARD MODEL

The FRG flow equations derived in Sec. D are suited for the weak-coupling limit [51]. In the dilute limit, however, when the Fermi energy scale becomes small compared to the interaction potential, the weak-coupling scenario may be violated. In order to convince ourselves that the approach produces meaningful results nevertheless, we benchmark the implementation against the mean-field solution of the Hubbard model at small densities.

To this end, we consider again the general Gaussian potential introduced in the main article and set $\ell = 0$, while fixing the prefactor to $g_0 = \frac{3}{2\pi}$. As displayed in Fig. 11, the characteristic temperature scale T_{\min} obtained from the FRG solution is in excellent agreement with the critical temperature as determined by the mean-field approach. Only at extremely low densities, below fillings relevant for our studies of geometric domes of T_c , deviations manifest. The FRG results remain consistent when a finite $\ell = 1$ is considered in the sense that the result smoothly connects to the Hubbard limit in the dilute limit where $k_F \ell \ll 1$. This is to be expected since the width of the Gaussian profile becomes large compared to the size of the Fermi surface and the interaction potential effectively appears almost constant.

-
- [1] G. R. Stewart, Heavy-fermion systems, *Rev. Mod. Phys.* **56**, 755 (1984).
- [2] Q. Si and F. Steglich, Heavy fermions and quantum phase transitions, *Science* **329**, 1161 (2010).
- [3] S. Wirth and F. Steglich, Exploring heavy fermions from macroscopic to microscopic length scales, *Nat. Rev. Mater.* **1**, 16051 (2016).
- [4] H.-H. Wen and S. Li, Materials and novel superconductivity in iron pnictide superconductors, *Annu. Rev. Condens. Matter Phys.* **2**, 121 (2011).
- [5] Q. Si, R. Yu, and E. Abrahams, High-temperature superconductivity in iron pnictides and chalcogenides, *Nat. Rev. Mater.* **1**, 16017 (2016).
- [6] R. M. Fernandes and A. V. Chubukov, Low-energy microscopic models for iron-based superconductors: A review, *Rep. Prog. Phys.* **80**, 014503 (2016).
- [7] M. N. Gastiasoro, J. Ruhman, and R. M. Fernandes, Superconductivity in dilute SrTiO₃: A review, *Ann. Phys.* **417**, 168107 (2020).
- [8] R. Russell, N. Ratcliff, K. Ahadi, L. Dong, S. Stemmer, and J. W. Harter, Ferroelectric enhancement of superconductivity in compressively strained SrTiO₃ films, *Phys. Rev. Materials* **3**, 091401 (2019).
- [9] M. N. Gastiasoro, T. V. Trevisan, and R. M. Fernandes, Anisotropic superconductivity mediated by ferroelectric fluctuations in cubic systems with spin-orbit coupling, *Phys. Rev. B* **101**, 174501 (2020).
- [10] S. Kanase and Y. Yanase, Multiorbital ferroelectric superconductivity in doped SrTiO₃, *Phys. Rev. B* **100**, 094504 (2019).
- [11] S. Kanase and Y. Yanase, Spin-orbit-coupled ferroelectric superconductivity, *Phys. Rev. B* **98**, 024521 (2018).

- [12] J. M. Edge, Y. Kedem, U. Aschauer, N. A. Spaldin, and A. V. Balatsky, Quantum Critical Origin of the Superconducting Dome in SrTiO₃, *Phys. Rev. Lett.* **115**, 247002 (2015).
- [13] K. Ahadi, L. Galletti, Y. Li, S. Salmani-Rezaie, W. Wu, and S. Stemmer, Enhancing superconductivity in SrTiO₃ films with strain, *Sci. Adv.* **5**, eaaw0120 (2019).
- [14] P. Wölfle and A. V. Balatsky, Superconductivity at low density near a ferroelectric quantum critical point: Doped SrTiO₃, *Phys. Rev. B* **98**, 104505 (2018).
- [15] S. E. Reyes-Lillo, K. M. Rabe, and J. B. Neaton, Ferroelectricity in [111]-oriented epitaxially strained SrTiO₃ from first principles, *Phys. Rev. Materials* **3**, 030601 (2019).
- [16] W. A. Atkinson, P. Lafleur, and A. Raslan, Influence of the ferroelectric quantum critical point on SrTiO₃ interfaces, *Phys. Rev. B* **95**, 054107 (2017).
- [17] Y. Kedem, J.-X. Zhu, and A. V. Balatsky, Unusual superconducting isotope effect in the presence of a quantum criticality, *Phys. Rev. B* **93**, 184507 (2016).
- [18] Y. Kedem, Novel pairing mechanism for superconductivity at a vanishing level of doping driven by critical ferroelectric modes, *Phys. Rev. B* **98**, 220505(R) (2018).
- [19] P. W. Anderson, P. A. Lee, M. Randeria, T. M. Rice, N. Trivedi, and F. C. Zhang, The physics behind high-temperature superconducting cuprates: The ‘plain vanilla’ version of RVB, *J. Phys.: Condens. Matter* **16**, R755 (2004).
- [20] B. Keimer, S. A. Kivelson, M. R. Norman, S. Uchida, and J. Zaanen, From quantum matter to high-temperature superconductivity in copper oxides, *Nature (London)* **518**, 179 (2015).
- [21] E. Berg, M. A. Metlitski, and S. Sachdev, Sign-problem-free quantum Monte Carlo of the onset of antiferromagnetism in metals, *Science* **338**, 1606 (2012).
- [22] D. Chowdhury and S. Sachdev, Higgs criticality in a two-dimensional metal, *Phys. Rev. B* **91**, 115123 (2015).
- [23] S. Raghu, G. Torroba, and H. Wang, Metallic quantum critical points with finite BCS couplings, *Phys. Rev. B* **92**, 205104 (2015).
- [24] Y. Wang, A. Abanov, B. L. Altshuler, E. A. Yuzbashyan, and A. V. Chubukov, Superconductivity Near a Quantum-Critical Point: The Special Role of the First Matsubara Frequency, *Phys. Rev. Lett.* **117**, 157001 (2016).
- [25] H. Wang, S. Raghu, and G. Torroba, Non-Fermi-liquid superconductivity: Eliashberg approach versus the renormalization group, *Phys. Rev. B* **95**, 165137 (2017).
- [26] E. Berg, S. Lederer, Y. Schattner, and S. Trebst, Monte Carlo studies of quantum critical metals, *Annu. Rev. Condens. Matter Phys.* **10**, 63 (2019).
- [27] D. Chowdhury and E. Berg, The unreasonable effectiveness of Eliashberg theory for pairing of non-Fermi liquids, *Ann. Phys.* **417**, 168125 (2020).
- [28] M. Randeria and E. Taylor, Crossover from Bardeen-Cooper-Schrieffer to Bose-Einstein condensation and the unitary Fermi gas, *Annu. Rev. Condens. Matter Phys.* **5**, 209 (2014).
- [29] G. C. Strinati, P. Pieri, G. Röpke, P. Schuck, and M. Urban, The BCS-BEC crossover: From ultra-cold Fermi gases to nuclear systems, *Phys. Rep.* **738**, 1 (2018).
- [30] M. N. Gastiasoro, A. V. Chubukov, and R. M. Fernandes, Phonon-mediated superconductivity in low carrier-density systems, *Phys. Rev. B* **99**, 094524 (2019).
- [31] J. Ruhman and P. A. Lee, Superconductivity at very low density: The case of strontium titanate, *Phys. Rev. B* **94**, 224515 (2016).
- [32] L. P. Gor’kov, Phonon mechanism in the most dilute superconductor n-type SrTiO₃, *Proc. Natl. Acad. Sci. USA* **113**, 4646 (2016).
- [33] L. P. Gor’kov, Back to mechanisms of superconductivity in low-doped strontium titanate, *J. Supercond. Nov. Magn.* **30**, 845 (2017).
- [34] N. E. Hussey, K. Takenaka, and H. Takagi, Universality of the Mott-Ioffe-Regel limit in metals, *Philos. Mag.* **84**, 2847 (2004).
- [35] E. Langmann, C. Triola, and A. V. Balatsky, Ubiquity of Superconducting Domes in the Bardeen-Cooper-Schrieffer Theory with Finite-Range Potentials, *Phys. Rev. Lett.* **122**, 157001 (2019).
- [36] K. Yang and S. L. Sondhi, Low-energy collective modes, Ginzburg-Landau theory, and pseudogap behavior in superconductors with long-range pairing interactions, *Phys. Rev. B* **62**, 11778 (2000).
- [37] L. Rademaker, Y. Wang, T. Berlijn, and S. Johnston, Enhanced superconductivity due to forward scattering in FeSe thin films on SrTiO₃ substrates, *New J. Phys.* **18**, 022001 (2016).
- [38] D.-H. Lee, Routes to high-temperature superconductivity: A lesson from FeSe/SrTiO₃, *Annu. Rev. Condens. Matter Phys.* **9**, 261 (2018).
- [39] M. M. Parish, B. Mihaila, E. M. Timmermans, K. B. Blagoev, and P. B. Littlewood, Bcs-bec crossover with a finite-range interaction, *Phys. Rev. B* **71**, 064513 (2005).
- [40] K. Yang, Superfluid-insulator transition and fermion pairing in Bose-Fermi mixtures, *Phys. Rev. B* **77**, 085115 (2008).
- [41] Properly speaking, we set $V(\mathbf{q})$ to be a periodic Gaussian, given by $V(\mathbf{q}) = -g_0(2\pi\ell)^{d/2} \sum_{\mathbf{G}} e^{-|\mathbf{q} + \mathbf{G}|^2\ell^2/2}$, where \mathbf{G} are reciprocal lattice vectors.
- [42] We define the arc length \mathcal{R} as $\int_{FS} |\mathcal{B}_{\ell^{-1}}(\mathbf{k}) \cap FS| d^{d-1}\mathbf{k}$ where the norm $|\cdot|$ is the geometric weight (the arc length in $d=2$ or the surface area in $d=3$) while $\mathcal{B}_{\ell^{-1}}(\mathbf{k})$ is a circle ($d=2$) or sphere ($d=3$) of fixed radius ℓ^{-1} centered around a point \mathbf{k}_F on the Fermi surface (FS).
- [43] The available phase space for scattering is primarily set by a momentum scale cutoff $\sim 1/\ell$, instead of by an explicit energy cutoff such as the Debye frequency in conventional BCS theory.
- [44] We define $k_F^* = (2\pi n^*)^{1/2}$ in 2D and $k_F^* = (3\pi^2 n^*)^{1/3}$ in 3D.
- [45] Y. Wang and A. V. Chubukov, Enhancement of superconductivity at the onset of charge-density-wave order in a metal, *Phys. Rev. B* **92**, 125108 (2015).
- [46] S. Lederer, Y. Schattner, E. Berg, and S. A. Kivelson, Enhancement of Superconductivity Near a Nematic Quantum Critical Point, *Phys. Rev. Lett.* **114**, 097001 (2015).
- [47] A. Klein, Y. Wu, and A. Chubukov, Multiple intertwined pairing states and temperature-sensitive gap anisotropy for superconductivity at a nematic quantum-critical point, *npj Quantum Mater.* **4**, 55 (2019).
- [48] W. Metzner, M. Salmhofer, C. Honerkamp, V. Meden, and K. Schönhammer, Functional renormalization group approach to correlated fermion systems, *Rev. Mod. Phys.* **84**, 299 (2012).
- [49] R. Gersch, C. Honerkamp, and W. Metzner, Superconductivity in the attractive Hubbard model: functional renormalization group analysis, *New J. Phys.* **10**, 045003 (2008).

- [50] A. Eberlein, Fermionic two-loop functional renormalization group for correlated fermions: Method and application to the attractive Hubbard model, *Phys. Rev. B* **90**, 115125 (2014).
- [51] C. Honerkamp and M. Salmhofer, Temperature-flow renormalization group and the competition between superconductivity and ferromagnetism, *Phys. Rev. B* **64**, 184516 (2001).
- [52] C. J. Halboth and W. Metzner, Renormalization-group analysis of the two-dimensional Hubbard model, *Phys. Rev. B* **61**, 7364 (2000).
- [53] The parameters are chosen such that they reproduce the superconducting T_c for the single-band Hubbard model, see Appendix E.
- [54] R. Micnas, J. Ranninger, and S. Robaszkiewicz, An extended Hubbard model with inter-site attraction in two dimensions and high-T_c superconductivity, *J. Phys. C: Solid State Phys.* **21**, L145 (1988).
- [55] The classification of phases in terms of the low-energy vertex structure is discussed, e.g., in Ref. [48].
- [56] Y. Kedem, Instability of a dilute fermi liquid in the presence of forward scattering, [arXiv:1904.11290](https://arxiv.org/abs/1904.11290).
- [57] A. G. Swartz, H. Inoue, T. A. Merz, Y. Hikita, S. Raghu, T. P. Devereaux, S. Johnston, and H. Y. Hwang, Polaronic behavior in a weak-coupling superconductor, *Proc. Natl. Acad. Sci. USA* **115**, 1475 (2018).
- [58] Z. Wang, S. McKeown Walker, A. Tamai, Y. Wang, Z. Ristic, F. Y. Bruno, A. de la Torre, S. Riccò, N. C. Plumb, M. Shi, P. Hlawenka, J. Sánchez-Barriga, A. Varykhalov, T. K. Kim, M. Hoesch, P. D. C. King, W. Meevasana, U. Diebold, J. Mesot, B. Moritz, T. P. Devereaux, M. Radovic, and F. Baumberger, Tailoring the nature and strength of electron–phonon interactions in the SrTiO₃(001) 2D electron liquid, *Nat. Mater.* **15**, 835 (2016).
- [59] C. Cancellieri, A. S. Mishchenko, U. Aschauer, A. Filippetti, C. Faber, O. S. Baršić, V. A. Rogalev, T. Schmitt, N. Nagaosa, and V. N. Strocov, Polaronic metal state at the LaAlO₃/SrTiO₃ interface, *Nat. Commun.* **7**, 10386 (2016).